Journal of Alloys and Compounds 478 (2009) 868–871

Contents lists available at ScienceDirect

Journal of Alloys and Compounds

journal homepage: www.elsevier.com/locate/jallcom

Effect of platinum present in multi-element nanoparticles on methanol oxidation

Chih-Fang Tsai, Kung-Yu Yeh, Pu-Wei Wu*, Yi-Fan Hsieh, Pang Lin

Department of Materials Science and Engineering, National Chiao Tung University, Hsin-Chu 30010, Taiwan, ROC

ARTICLE INFO

Article history:
Received 12 August 2008
Received in revised form
29 November 2008
Accepted 13 December 2008
Available online 25 December 2008

Keywords:
Fuel cells
Nanostructured materials
Catalysis
Methanol oxidation

ABSTRACT

Nanoparticles of $Pt_xFe_{(100-x)/5}Co_{(100-x)/5}Ni_{(100-x)/5}Cu_{(100-x)/5}Ag_{(100-x)/5}$ (x = 22, 29, 52, 56) were prepared by the sputter depositions on pretreated carbon clothes with their electrocatalytic abilities for the methanol oxidation investigated. XRD analysis of the deposited nanoparticles indicated crystalline fcc phases and SEM images revealed apparent growths of nanoparticulate nodules. Their average sizes were found to increase with the deposition time. Cyclic voltammetry of the deposited samples demonstrated enhancements in the current responses with increasing Pt amount and deposition time. In mass activity, the $Pt_{52}Fe_{11}Co_{10}Ni_{11}Cu_{10}Ag_8$ exhibited the highest values of 462–504 mA/mg. Identical process was conducted to fabricate electrodes with sputtered Pt and $Pt_{43}Ru_{57}$. In comparison, the $Pt_{52}Fe_{11}Co_{10}Ni_{11}Cu_{10}Ag_8$ showed moderate improvements over that of Pt but was still outperformed by the $Pt_{43}Ru_{57}$.

1. Introduction

Rising demands of portable electronics create greater requirements for power systems with extended operation time. Due to their high energy density as well as simplicity in fuel storage and transportation, the direct methanol fuel cells (DMFC) have received considerable attention recently as the possible solution to replace lithium-ion batteries. The operation of DMFC involves methanol electrooxidation in an acidic electrolyte. Therefore, potential electrocatalysts must exhibit acceptable corrosion resistances, a character that can only be found in noble metals. Due to the CO adsorption after methanol dehydrogenation, the Pt is deactivated rapidly as an anode electrocatalyst [1]. Hence, additional elements are necessary in alloying with the Pt to facilitate CO oxidation [2]. For example, alloys in binary, tertiary, and quaternary compositions such as PtRu, PtCo, PtRuCo, and PtRuNiZr have been studied with reasonable successes [3–7]. Among them, the PtRu exhibits the highest electrocatalytic performance and is widely used for DMFC demonstrations [8]. However, from practical considerations it is desirable to replace Ru with less-expensive metals. As a result, substantial activities are still engaged in pursuing materials with unique constituents to obtain comparable catalytic behaviors.

The concept of alloy formation based on multiple principal elements was first proposed by Yeh et al., in which more than six components at equimolar or near-equimolar ratios (e.g. $CuCoNiCrAl_xFe$, MoTiVFeNiZrCoCr) were melted and solidified in a solid solution [9]. Due to a large increase in the mixing entropy, the alloys with multiple components reveal unusual characteristics which are contradictory to what would be expected from conventional metallurgies. Instead of formation in distinctive intermetallic compounds, they are more likely to exist in solid solutions of fcc and bcc, or are simply amorphous [10]. So far, substantial enhancements in mechanical strength, high temperature oxidation, and corrosion resistance have been demonstrated by the multi-element alloys at various compositions. Typical fabrication of the multi-element alloys employs conventional metallurgical approaches in which bulk materials are prepared and analyzed. On the other hand, synthesis of the "multi-element nanoparticles" is relatively unknown.

Chemical reductions to synthesize nanoparticles with multiple elements are especially challenging because the redox potentials in individual elements vary considerably and full control of the resulting compositions is nearly impossible. In contrast, the sputter deposition is established to produce films with tailored compositions and its fabrication step is straightforward. Previously, the sputter deposition was shown to produce nanosized clusters exhibiting exceptionally high rates in the catalyst utilization for fuel cell applications [11]. For example, Caillard et al. reported that codeposition of Pt and Ru lead to an alloy phase of Pt_xRu_{1-x} and determined the optimum composition to be 30–40% of Ru [12]. Similar results were documented by O'Hayre et al. [13] and Haug et al. [14]. Recently, we obtained nanoparticles by sputter deposition in composition of $Pt_{50}Fe_{11}Co_{10}Ni_{11}Cu_{10}Ag_8$ and reported interesting catalytic behaviors for the methanol oxidation [15]. However,

* Corresponding author. Tel.: +886 3 5131227; fax: +886 3 5724727.
E-mail address: ppwu@mail.nctu.edu.tw (P.-W. Wu).

0925-8388/$ – see front matter © 2008 Elsevier B.V. All rights reserved.
doi:10.1016/j.jallcom.2008.12.055

the optimized Pt amount for the highest methanol electrooxidation ability was not determined.

In this work, we report the preparations and characterizations of multi-element nanoparticles and investigate their catalytic abilities as a function of the Pt amount. The compositions studied were $Pt_xFe_{(100-x)/5}Co_{(100-x)/5}Ni_{(100-x)/5}Cu_{(100-x)/5}Ag_{(100-x)/5}$ with $x = 22$, 29, 52, and 56, respectively.

2. Experimental

2.1. Preparation of the multi-element nanoparticles

Radio frequency sputter depositions were conducted to prepare the multi-element nanoparticles on commercially available carbon clothes (E-TEK). Prior to the sputter deposition, the carbon cloth (4 cm × 4 cm) was precoated with a dispersion of 70 wt% Shawinigan Acetylene Black (Chevron) and 30 wt% PTFE (DuPont) to reach a dry weight of 22 mg/cm^2. The target material for the sputter operation was a mixture of metal powders including Fe (10.3 μm), Co (1.4 μm), Ni (2.5 μm), Cu (45.0 μm), and Ag (0.8 μm) at a molar ratio of 24:22:21:15:18. The mixture underwent a dry tumbling process for 24 h with 25 g in each batch, followed by a hydraulic pressing at 2500 psi for 30 s to make a disk with 3.0 inch in diameter. In order to add Pt into the deposition flux, foils of Pt (99.9%, 1 cm × 1 cm) were positioned on top of the target disk. The number and location of those Pt foils were explored to obtain nanoparticles with the desirable compositions. For proper determinations in phases and lattice parameters, SiO_2 (1 cm × 1 cm) was used as the substrate for growth of the alloy films. During the process, the carbon cloth and SiO_2 reference substrate were subjected to a rotating motion to ensure uniform depositions. The schematic for the sputter deposition setup can be found elsewhere [15].

2.2. Materials characterizations and electrochemical analysis

An XRD with CuKα radiation (λ = 1.5418 Å) (Siemens D5000) was used to identify relevant phases present for the deposited alloy films. Morphologies of the nanoparticles on the carbon clothes were observed by SEM (JSM-6500F). An Energy Dispersive X-ray Spectroscope (EDX) was employed on the SiO_2 substrates to determine the exact composition of alloy films. The thickness of the deposited films was measured by an α stepper (Dektak 3ST) at various times to estimate the deposition rate. Electrochemical characterizations were carried out at room temperature in cyclic voltammogram (CV) using a Solartron SI 1287 potentiostat with 500 ml aqueous electrolyte containing 0.5 M H_2SO_4 and 1.0 M CH_3OH. Prior to the electrochemical measurements, the electrolyte was purged with nitrogen for 15 min and waited for 30 min, allowing stabilization of the open circuit voltage. The carbon cloth loaded with electrocatalysts (0.87 cm^2) was used as the working electrode. The Ag/AgCl was used as the reference electrode and Pt foil was used as the counter electrode. The CVs were analyzed in a range of 0–0.95 V vs. reference electrode at a scan rate 50 mV/s.

3. Results and discussion

3.1. Characterizations of nanoparticles

By careful preparations of the target materials, we were able to obtain the deposited films at compositions of $Pt_{22}Fe_{14}Co_{15}Ni_{14}Cu_{18}Ag_{17}$, $Pt_{29}Fe_{14}Co_{15}Ni_{15}Cu_{13}Ag_{14}$, $Pt_{52}Fe_{11}Co_{10}Ni_{11}Cu_{10}Ag_8$, and $Pt_{56}Fe_7Co_8Ni_{10}Cu_9Ag_{10}$. Fig. 1 exhibits the XRD patterns of the alloy films deposited on the carbon clothes for 120 min. We chose 120 min because at a shorter duration the signals from the carbon cloth would compromise diffraction peaks from the multi-element films. It was determined that crystalline phases of fcc were present for all samples. Judging by the intensity of the (1 1 1) peaks, the crystallinity of the alloy films was found to deteriorate with decreasing Pt amount. This inferred that the presence of Pt was beneficial for the formation of fcc phase. The relatively high level of noises in the XRD patterns was attributed to the carbon cloth. Table 1 lists the exact compositions and phases for the deposited films on the SiO_2 substrate after 120 min of deposition. Since the atomic radii of Fe, Co, Ni, and Cu are much smaller than that of Pt, the lattice parameters of the deposited alloy films increased with increasing Pt amount as expected.

Fig. 2 presents the representative SEM pictures of the carbon cloth and $Pt_{56}Fe_7Co_8Ni_{10}Cu_9Ag_{10}$ after deposition for 5 min. Clearly shown in Fig. 2(a), the carbon cloth exhibited aggregations of car-

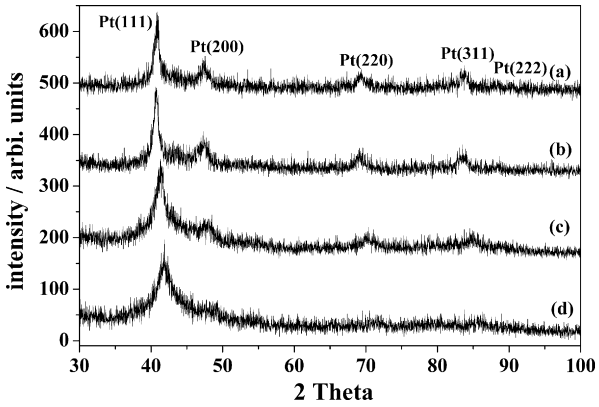

Fig. 1. X-ray diffraction patterns for the carbon clothes deposited with 120 min of the multi-element alloy films at compositions of (a) $Pt_{56}Fe_7Co_8Ni_{10}Cu_9Ag_{10}$, (b) $Pt_{52}Fe_{10}Co_9Ni_9Cu_{12}Ag_8$, (c) $Pt_{29}Fe_{14}Co_{15}Ni_{15}Cu_{13}Ag_{14}$, and (d) $Pt_{22}Fe_{14}Co_{15}Ni_{14}Cu_{18}Ag_{17}$.

Table 1
Characteristics of multi-element alloy films after X-ray and EDX analysis.

Composition[a]	Lattice parameter (Å)[b]	Crystal structure[b]
$Pt_{22}Fe_{14}Co_{15}Ni_{14}Cu_{18}Ag_{17}$	3.74	FCC
$Pt_{29}Fe_{14}Co_{15}Ni_{15}Cu_{13}Ag_{14}$	3.77	FCC
$Pt_{52}Fe_{11}Co_{10}Ni_{11}Cu_{10}Ag_8$	3.83	FCC
$Pt_{56}Fe_7Co_8Ni_{10}Cu_9Ag_{10}$	3.86	FCC

[a] From EDS.
[b] From XRD.

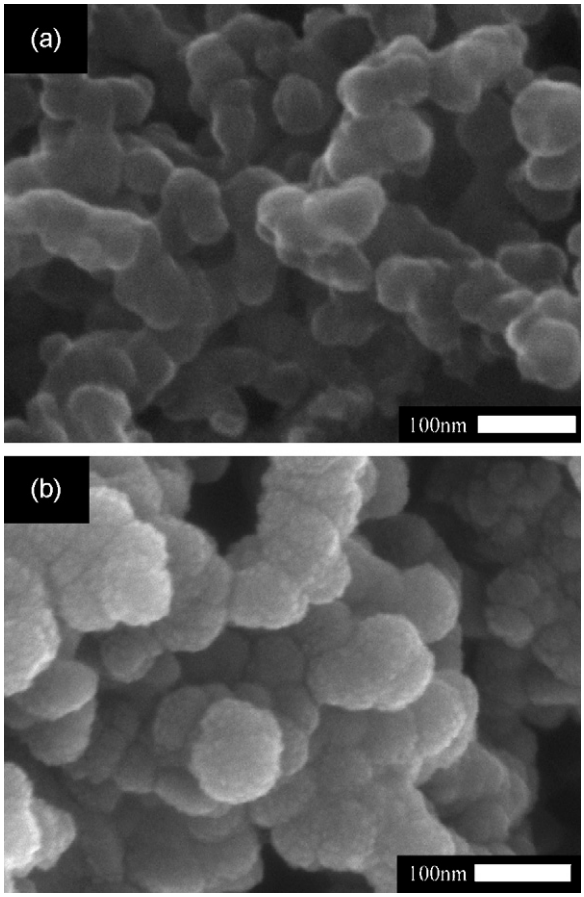

Fig. 2. SEM images of (a) carbon clothes before the sputter deposition and (b) 5 min deposition of $Pt_{56}Fe_7Co_8Ni_{10}Cu_9Ag_{10}$.

bon particles in irregular shapes approximately 50 nm in sizes. After deposition for 5 min shown in Fig. 2(b), much larger particles with average sizes of 90 nm were observed. In addition, there were appearances of nodules on the carbon surfaces with preliminary coalescence taking place. Similar morphologies were observed at particles with less deposition times. From the SEM pictures taken at various deposition times, the growth of nanoparticles agreed reasonably to the estimated deposition rate of 8.4 nm/min for the $Pt_{56}Fe_7Co_8Ni_{10}Cu_9Ag_{10}$.

3.2. Effects of the deposition time on CV responses

The CVs of the deposited nanoparticles were analyzed carefully for their electrocatalytic abilities for the methanol oxidation. In our systems, the CV responses improved gradually upon cycling and stabilized after 50 cycles. Hence, the CV scan at the 100th cycle was used for catalytic evaluations. Fig. 3 presents the results for the $Pt_{56}Fe_7Co_8Ni_{10}Cu_9Ag_{10}$ after deposition time of 2, 3, and 5 min, respectively. We selected those parameters because in our earlier work we observed a gradual decrease in the mass activity when the deposition time was prolonged [15]. During the anodic scans, the peak potentials of 2, 3, and 5 min appeared at 0.671 V, 0.676 V, and 0.706 V, respectively. Likewise, the peak potentials from the cathodic scans were located at 0.504 V, 0.518 V, and 0.546 V, respectively. The potentials for the anodic and cathodic peaks seem to increase with the deposition time. In addition, the onset potentials for the methanol electrooxidation were determined at 0.223 V, 0.222 V, and 0.202 V for 2, 3, and 5 min, respectively. The peak current and area under the CV curves were found to be proportional to the loadings of the electrocatalyst as expected.

3.3. Effect of the Pt amount on CV responses

Fig. 4 presents the CV responses for the $Pt_{22}Fe_{14}Co_{15}Ni_{14}Cu_{18}Ag_{17}$, $Pt_{29}Fe_{14}Co_{15}Ni_{15}Cu_{13}Ag_{14}$, $Pt_{52}Fe_{11}Co_{10}Ni_{11}Cu_{10}Ag_8$, and $Pt_{56}Fe_7Co_8Ni_{10}Cu_9Ag_{10}$ after 3 min of deposition. They corresponded to catalyst loadings of 0.027, 0.033, 0.024, and 0.039 mg/cm^2, respectively. We obtained the catalyst amounts by multiplying the theoretic density (from X-ray) with the deposited volume. Since we knew the exact area for the sputter deposition, the deposited volume could be acquired by determining the deposition rate, which was estimated by depositions at intervals of 30, 40, and 120 min, respectively. We rationalized that the variations in the catalyst loadings resulted from the difference in the sputtering yield of individual elements. The CV profiles showed obvious current responses for both anodic and cathodic scans, which are

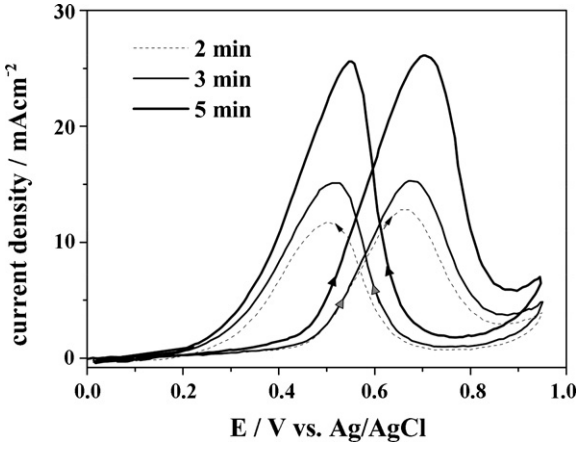

Fig. 3. Cyclic voltammetry curves of the $Pt_{56}Fe_7Co_8Ni_{10}Cu_9Ag_{10}$ deposited for 2, 3, and 5 min, respectively.

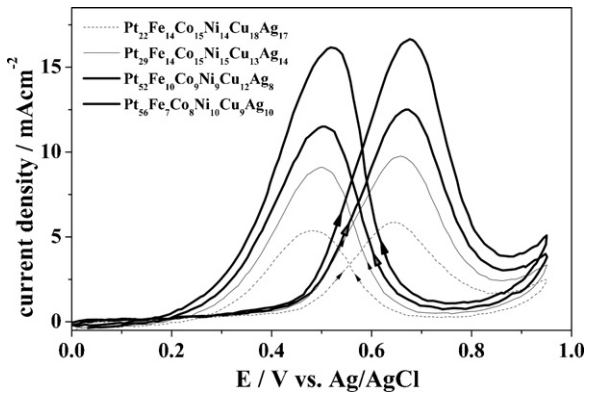

Fig. 4. Cyclic voltammetry curves of $Pt_{56}Fe_7Co_8Ni_{10}Cu_9Ag_{10}$, $Pt_{52}Fe_{10}Co_9Ni_9Cu_{12}Ag_8$, $Pt_{29}Fe_{14}Co_{15}Ni_{15}Cu_{13}Ag_{14}$, and $Pt_{22}Fe_{14}Co_{15}Ni_{14}Cu_{18}Ag_{17}$ at the 100th cycle.

consistent with what were reported earlier for the Pt based alloy electrocatalysts [16]. In addition, the peak current densities for both scans improved with increasing Pt amounts. However, the onset potentials and potentials at maximum forward and backward scans increased slightly with increasing Pt amount, inferring gradual reduction of the intrinsic catalytic abilities.

The peak current densities for both forward and backward scans are represented by i_f and i_b, respectively. Typically, the value of i_f/i_b indicates the catalytic ability to remove CO after methanol dehydrogenation. Table 2 lists details of the electrochemical parameters from the CV scans for our nanoparticles. To our disappointment, there was negligible difference in values of i_f/i_b. This unusual insensitivity to composition variations is a notable contrast to earlier reports by Deivaraj and Lee [17] as well as Liu et al. [18]. For example, Deivaraj and Lee identified the i_f/i_b of 0.96–1.40 in their study of PtRu. We believe that varying degrees of anodic dissolutions of Fe, Co, Ni, Cu, and Ag were occurring during the CV scans that rendered uncharacteristic Pt-rich surfaces for all our samples. In contrast, the values of i_f/i_b for the sputtered Pt and $Pt_{43}Ru_{57}$ were measured at 0.88 and 1.57, respectively. Despite failing to compete with the $Pt_{43}Ru_{57}$, the multi-element nanoparticles still maintained moderate improvements over that of Pt. To identify the mechanism of anodic dissolutions, current activities in our laboratory are focused on controlling the amount of anodic dissolution to prepare nanoparticles with much enhanced electrochemical active areas.

Due to the variations in deposition rate and resulting catalyst loading, accurate determination of the catalytic performances could only be obtained if mass activities (mA/mg) are benchmarked. The values for mass activities, shown in Fig. 5, were found to

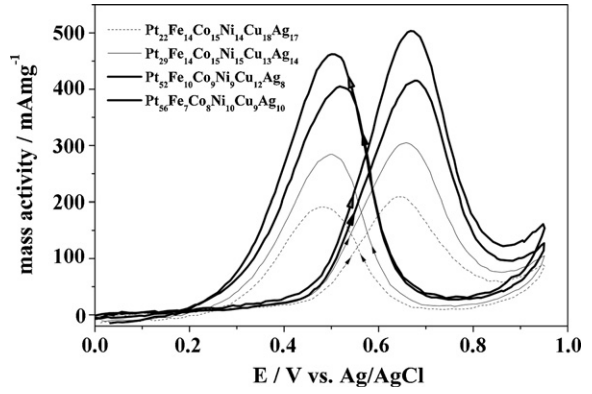

Fig. 5. Cyclic voltammetry curves in mass activities of $Pt_{56}Fe_7Co_8Ni_{10}Cu_9Ag_{10}$, $Pt_{52}Fe_{10}Co_9Ni_9Cu_{12}Ag_8$, $Pt_{29}Fe_{14}Co_{15}Ni_{15}Cu_{13}Ag_{14}$, and $Pt_{22}Fe_{14}Co_{15}Ni_{14}Cu_{18}Ag_{17}$ at the 100th cycle.

Table 2
Electrochemical parameters of multi-element nanoparticles, Pt, and $Pt_{43}Ru_{57}$ from the CV responses at the 100th cycle.

	Onset potential (V)	Potential (V) at i_f	i_f (mA/cm^2)[a]	Potential (V) at i_b	i_b (mA/cm^2)[b]	i_f/i_b
$Pt_{22}Fe_{14}Co_{15}Ni_{14}Cu_{18}Ag_{17}$	0.217	0.640	5.85	0.479	5.37	1.09
$Pt_{29}Fe_{14}Co_{15}Ni_{15}Cu_{13}Ag_{14}$	0.223	0.658	9.76	0.501	9.11	1.07
$Pt_{52}Fe_{11}Co_{10}Ni_{11}Cu_{10}Ag_8$	0.228	0.668	12.50	0.501	11.48	1.09
$Pt_{56}Fe_7Co_8Ni_{10}Cu_9Ag_{10}$	0.222	0.676	16.62	0.518	16.20	1.02
Pt	0.180	0.684	18.04	0.549	20.53	0.88
$Pt_{43}Ru_{57}$	0.089	0.677	14.03	0.486	8.93	1.57

[a] Peak current density at forward scan.
[b] Peak current density at backward scan.

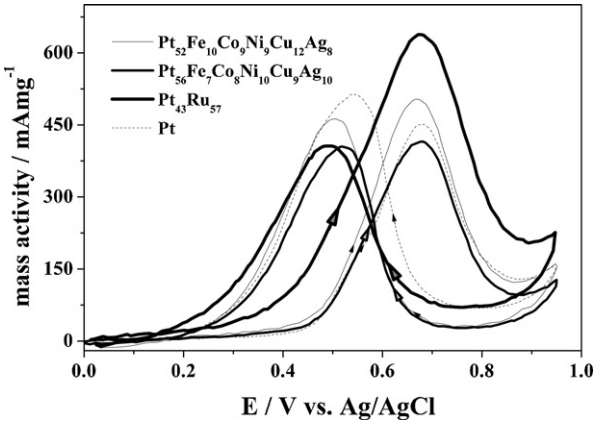

Fig. 6. Cyclic voltammetry curves in mass activities of $Pt_{56}Fe_7Co_8Ni_{10}Cu_9Ag_{10}$, $Pt_{52}Fe_{10}Co_9Ni_9Cu_{12}Ag_8$, Pt, and $Pt_{43}Ru_{57}$ at the 100th cycle.

increase with the increasing Pt amount, reaching the highest values at $Pt_{52}Fe_{10}Co_9Ni_9Cu_{12}Ag_8$. Interestingly, the mass activities of $Pt_{56}Fe_7Co_8Ni_{10}Cu_9Ag_{10}$ exhibited obvious reductions in catalytic performances. However, we would like to emphasize that for $Pt_{52}Fe_{10}Co_9Ni_9Cu_{12}Ag_8$ and $Pt_{56}Fe_7Co_8Ni_{10}Cu_9Ag_{10}$ the mass activities were in the range of 400–500 mA/mg, values that agree with what were reported previously [19]. The loss of catalytic ability for the $Pt_{56}Fe_7Co_8Ni_{10}Cu_9Ag_{10}$ could be simply due to its larger particle sizes.

The sputter depositions were also performed to obtain the nanoparticles of Pt and $Pt_{43}Ru_{57}$. The deposition rates for the Pt and $Pt_{43}Ru_{57}$ were 6.3 nm/min (0.014 mg min^{-1} cm^{-2}) and 4.6 nm/min (0.007 mg min^{-1} cm^{-2}), respectively. Following the identical methodologies we analyzed their CV responses in mass activities and plotted their values (in Fig. 6) along with those from the $Pt_{52}Fe_{10}Co_9Ni_9Cu_{12}Ag_8$ and $Pt_{56}Fe_7Co_8Ni_{10}Cu_9Ag_{10}$. Apparently, the CV curve from the $Pt_{43}Ru_{57}$ exhibited the highest mass activity, consistent with a well-established fact that the 1:1 ratio of Pt:Ru is desirable. With moderate reductions in catalytic ability as compared to that of $Pt_{43}Ru_{57}$, the $Pt_{52}Fe_{10}Co_9Ni_9Cu_{12}Ag_8$ still maintained a notable enhancement over that of Pt. This suggests the possibility in exploring these multi-element nanoparticles in other Pt-based catalytic applications.

4. Conclusions

The sputter depositions were employed to fabricate nanoparticles of $Pt_{22}Fe_{14}Co_{15}Ni_{14}Cu_{18}Ag_{17}$, $Pt_{29}Fe_{14}Co_{15}Ni_{15}Cu_{13}Ag_{14}$, $Pt_{52}Fe_{11}Co_{10}Ni_{11}Cu_{10}Ag_8$, as well as $Pt_{56}Fe_7Co_8Ni_{10}Cu_9Ag_{10}$ for methanol electrooxidation. XRD analysis of the deposited samples confirmed crystalline phases of fcc and SEM observations revealed growths of nodules in commensurate with the deposition times. The CV responses suggested improvements in performances with increasing Pt amount. However, in mass activities the $Pt_{52}Fe_{11}Co_{10}Ni_{11}Cu_{10}Ag_8$ was found to demonstrate the highest catalytic abilities. In comparison, the $Pt_{52}Fe_{11}Co_{10}Ni_{11}Cu_{10}Ag_8$ showed improved characteristics over Pt but was outperformed by $Pt_{43}Ru_{57}$. We believe the sputter deposition provides a rapid synthetic approach to prepare multi-element nanoparticles for possible synergistic effects. Once proper compositions are identified, typical chemical reduction route could be implemented accordingly.

Acknowledgements

Equipment assistances from Professor Chiun-Hsun Chen of Mechanical Engineering Department and guidance in multi-element alloy formations from Professor Cheun-Guang Chao of Materials Science and Engineering Department are highly appreciated.

References

[1] Y. Zhu, H. Uchida, T. Yajima, M. Watanabe, Langmuir 17 (2001) 146.
[2] J.Y. Kim, Z.G. Yang, C.C. Chang, T.I. Valdez, S.R. Narayanan, P.N. Kumta, J. Electrochem. Soc. 150 (2003) A1421.
[3] Z. Wang, G. Chen, D. Xia, L. Zhang, J. Alloys Compounds 450 (2008) 148.
[4] C. Wang, D. Wang, X. Hu, C. Dai, L. Zhang, J. Alloys Compounds 448 (2008) 109.
[5] E. Antolini, J.R.C. Salgado, E.R. Gonzalez, J. Electroanal. Chem. 580 (2005) 145.
[6] P. Strasser, Q. Fan, M. Devenney, W.H. Weinberg, P. Liu, J.K. Nørskov, J. Phys. Chem. B 107 (2003) 11013.
[7] J.F. Whitacre, T. Valdez, S.R. Narayanan, J. Electrochem. Soc. 152 (2005) A1780.
[8] X. Li, I.M. Hsing, Electrochim. Acta 52 (2006) 1358.
[9] J.W. Yeh, S.K. Chen, S.J. Lin, J.Y. Gan, T.S. Chin, T.T. Shun, C.H. Tsau, S.Y. Chang, Adv. Eng. Mater. 6 (2004) 299.
[10] C.J. Tong, Y.L. Chen, W.K. Chen, J.W. Yeh, T.T. Shun, C.H. Tsau, S.J. Lin, S.Y. Chang, Metallurg. Mater. Trans. A 36A (2005) 881.
[11] S.Y. Cha, W.M. Lee, J. Electrochem. Soc. 146 (1999) 4055.
[12] A. Caillard, C. Coutanceau, P. Brault, J. Matias, J.M. Léger, J. Power Sources 162 (2006) 66.
[13] R. O'Hayre, S.J. Lee, S.W. Cha, F.B. Prinz, J. Power Sources 109 (2002) 483.
[14] A.T. Haug, R.E. White, J.W. Weidner, W. Huang, S. Shi, T. Stoner, N. Rana, J. Electrochem. Soc. 149 (2002) A280.
[15] C.F. Tsai, P.W. Wu, P. Lin, C.G. Chao, K.Y. Yeh, Jpn. J. Appl. Phys. 47 (2008) 5755.
[16] Z.B. Wang, G.P. Yin, J. Zhang, Y.C. Sun, P.F. Shi, Electrochim. Acta 51 (2006) 5691.
[17] T.C. Deivaraj, J.Y. Lee, J. Power Sources 142 (2005) 43.
[18] Z. Liu, M. Shamsuzzoha, E.T. Ada, W.M. Reichert, D.E. Nakles, J. Power Sources 164 (2007) 472.
[19] M. Alvisi, G. Galtieri, L. Giorgi, R. Giorgi, E. Serra, M.A. Signore, Surf. Coat. Tech. 200 (2005) 1325.